The Astrophysical Journal, 957:110 (9pp), 2023 November 10 https://doi.org/10.3847/1538-4357/acf8bf

Multi-spacecraft Observations of the 2022 March 25 CME and EUV Wave: An Analysis of Their Propagation and Interrelation

Alessandro Liberatore[1], Paulett C. Liewer[1], Angelos Vourlidas[2], Carlos R. Braga[3], Marco Velli[1,4,5], Olga Panasenco[6], Daniele Telloni[7], and Salvatore Mancuso[7]
[1] Jet Propulsion Laboratory, California Institute of Technology, Pasadena, CA 91109, USA; alessandro.liberatore@jpl.nasa.gov
[2] The Johns Hopkins University Applied Physics Laboratory, Laurel, MD 20723, USA
[3] George Mason University, Fairfax, VA 22030, USA
[4] Department of Earth, Planetary, and Space Sciences, University of California, Los Angeles, CA, 90095 USA
[5] International Space Science Institute, 3012 Bern, Switzerland
[6] Advanced Heliophysics, Pasadena, CA 91106, USA
[7] National Institute for Astrophysics, Astrophysical Observatory of Turin, I-10025, Pino To.se, Turin, Italy
Received 2023 July 11; revised 2023 August 22; accepted 2023 September 4; published 2023 November 6

Abstract

This paper reports on a well-defined EUV wave associated with a coronal mass ejection (CME) observed on 2022 March 25. The CME was observed by Solar Orbiter (SolO) during its first close perihelion (0.32 au) and by several other spacecraft from different viewpoints. The EUV wave was visible by the Extreme Ultraviolet Imager on board the Solar Terrestrial Relations Observatory (STEREO-A/STA) in near quadrature to SolO. We perform a detailed analysis of the early phase of this CME in relation to the evolution of the associated EUV wave. The kinematics of the EUV wave and CME are derived via visual identification of the fronts using both the STA and SolO data. The analysis of an associated metric type II radio burst provides information on the early phase of the CME and wave propagation. Finally, we compare the EUV speed to the local magnetic field and Alfvén speed using standard models of the corona. The analysis of the decoupling between the EUV wave and the CME driver via imaging, kinematic study, radio data analysis, and comparison with maps/models clearly indicates that the EUV front is consistent with a wave initially driven by the lateral expansion of the CME, which evolves into a fast-mode magnetosonic wave after decoupling from the CME.

Unified Astronomy Thesaurus concepts: Solar physics (1476); The Sun (1693); Solar extreme ultraviolet emission (1493); Solar coronal mass ejections (310)

Supporting material: animation

1. Introduction

On 2022 March 25, during the first close Solar Orbiter (SolO) perihelion, several remote-sensing instruments on board SolO observed a coronal mass ejection (CME) erupting from the east solar limb. Other spacecraft (S/C) observed the same event from different viewpoints. Figure 1 gives an overview of the relative position of some S/C in the period of interest. The Extreme Ultraviolet Imager (EUVI) on board the Solar Terrestrial Relations Observatory (STEREO-A/STA), in quadrature with SolO (≈98°), observed a well-defined extreme-ultraviolet (EUV) wave propagating away from the active region (AR) associated with the observed CME.

EUV waves are large-scale wavelike coronal disturbances visible in EUV light, first reported by Thompson et al. (1999) using observations by the Extreme ultraviolet Imaging Telescope (EIT; Delaboudinière et al. 1995) on board the Solar and Heliospheric Observatory (SOHO). Since then, there have been many studies of the phenomena (Patsourakos & Vourlidas 2012; Long et al. 2017 and references therein). EUV waves are almost always associated with CMEs (Biesecker et al. 2002; Cliver et al. 2005). After the launches of STEREO and the Solar Dynamics Observatory (SDO), with a higher cadence in the EUV instruments and quadrature observations, it became possible to take a closer look at the relationship between these two phenomena (Kienreich et al. 2009; Patsourakos & Vourlidas 2009; Dai et al. 2012; Patsourakos & Vourlidas 2012).

In this paper, we investigate the nature of EUV waves in relation to the CME evolution through the analysis of the multi-S/C remote-sensing observations of the 2022 March 25 events. We compare with the scenario in Patsourakos & Vourlidas (2009) and Kienreich et al. (2009), in which an initially driven EUV disturbance evolves to become a freely propagating fast-mode wave. A kinematic analysis on both the CME and EUV wavefront evolution, performed via a point-and-click method, gave us important information on the interrelation between the two phenomena early in their evolution (Section 3). The analysis of a type II radio burst detected by the analysis of radio data provides key information on the rapid expansion of the CME front and the EUV wave propagation. Finally, the comparison of the EUV wavefront expansion with the local magnetic field and the Alfvén-velocity gives additional support for our interpretation on the nature of the wave (Section 4).

2. The 2022 March 25 CME

On 2022 March 25 at 05:00 UTC, multiple S/C observed a CME originating from AR 12974. SolO followed the CME during its entire evolution from the low corona to large heliocentric distances (>55 $R_\odot$) by combining three remote-sensing instruments on board: the Full Sun Imager (FSI-174; Rochus et al. 2020), the coronagraph Metis (Antonucci et al. 2020), and the

SolO Heliospheric Imager (SoloHI; Howard et al. 2020). SoloHI images are a composite of four tiles. The field of view (FOV) elongation (i.e., angle from the Sun) range of the instrument is 5.°4–44.°9 to the east of the Sun and ≈±20° on the transverse direction (Howard et al. 2020). Figure 2 shows composite images acquired by the different instruments on board SolO.

Because SolO and STA were near quadrature during this period, the same CME observed on the plane of sky by SolO appears as a halo CME to the Coronagraph 2 (COR2) on board STA. STA/COR2 and the Large Angle Spectrometric Coronagraph (LASCO-C2/C3) observe the CME after it emerges from behind their occulters at $2\,R_{\odot}$ and 1.5–3.7 $R_{\odot}$, respectively (Figure 3). Considering the three different points of view provided by SoloHI, STA/COR2, and LASCO/C3 (cf. Figure 1) it was possible to determine the CME geometry and trajectory. During its propagation, the CME was detected by in situ instruments on board Bepi-Colombo, STEREO-A, and at the first Lagrangian point (L1)–Earth S/C. A detailed study of the CME evolution from a geometrical, kinematic, and in situ analysis will be discussed separately.

In this paper, we focus more on the initial phase of the CME and its interrelation with EUV wave propagation. It is difficult to extract information on the initial phase of the CME from either the STA or SOHO positions because it is evolving in an optically thin corona with the solar disk in the background. On the other hand, the early phases of this CME are visible by SolO/FSI because of its advantageous position with respect to STA. Due to the low 10 minute cadence of FSI during these acquisitions, the best estimate of the CME starting time is 05:00-05:10 UTC. We estimated the CME front velocity moving from FSI to Metis to SoloHI through a point-and-click method, obtaining $v \approx 500$–$600\ \mathrm{km\ s^{-1}}$.

3. EUV Wave Observation and Analysis

During the 2022 March 25 CME, both the STA/EUVI and SolO/FSI observed an EUV wave propagating away from the AR 12974 on the solar disk (Figures 4 and 5, respectively). In the following, we introduce the main aspects of the EUV wave and the analysis performed on the EUV wavefront propagation and its relation to the expanding CME.

3.1. About the Nature of the EUV Waves

The EUV waves are large-scale wavelike coronal disturbances visible in EUV light and propagating away from eruptive ARs. Patsourakos & Vourlidas (2012) review various interpretations of the nature of EUV waves as pseudo-waves, magnetohydrodynamic (MHD) waves, or hybrid (i.e., a combination of both pseudo-waves and true MHD wave). The pseudo-wave interpretation suggests that EUV waves are the disk projection of the CME's expanding envelope and not a true wave phenomenon (Delannée & Aulanier 1999). The fast-/slow-mode MHD wave mode speeds can be described by the following equation:

$$v_{f,s}^2 = \frac{1}{2}(v_A^2 + c_s^2 \pm \sqrt{(v_A^2 + c_s^2)^2 - 4c_s^2 v_A^2 \cos^2\theta}), \qquad (1)$$

where v_A and c_s are the local Alfvén and sound speeds, respectively, and θ is the inclination between the wavevector and magnetic field B. From Equation (1), it is clear that the fast-mode wave velocity (v_f) is weakly dependent on the direction of the magnetic field. On the other hand, the slow-mode phase velocity (v_s) has a strong dependence on propagation angle and goes to zero at $\theta = 90°$ (i.e., it cannot propagate perpendicularly to the magnetic field lines). The group velocity is also limited to a narrow cone around the magnetic field direction. For this reason, slow-mode wave interpretation is often rejected because of the relatively large angular extent over large scales of these phenomena. Equation (1) shows also that a fast magnetosonic wave must have a speed $> v_A$.

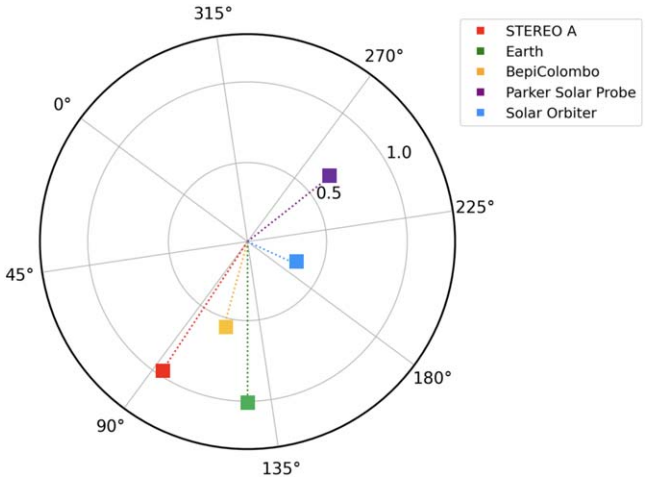

Figure 1. Relative position of the S/C on 2022 March 25 at 05:00:00 am UTC (Gieseler et al. 2023). STEREO-A (red square) and SolO (blue square) are near quadrature.

Patsourakos & Vourlidas (2012) describe in detail how the EUV waves can be interpreted as waves initially driven by a fast lateral expansion of the CME, then transitioning to a (true) fast magnetosonic wave, at a lower velocity, after the rapid initial expansion slows. Typical velocities of the freely propagating wave are around $200\ \mathrm{km\ s^{-1}}$. Patsourakos & Vourlidas (2012) note that the observation of this kinematic behavior is almost impossible without high-cadence (≈1 minute) imaging since the initial high-speed propagation and the decoupling phase tend to develop within 5 minutes or so.

3.2. EUV Wave Associated with the Observed CME

The EUV wave associated with the 2022 March 25 CME was observed by STA/EUVI propagating away from the eruptive AR 12974 placed almost at the center of the EUVI FOV at Carrington coordinates (LN, LT) = (87°, −22°). We used EUVI-195 images to perform a running difference of the EUV wave. The wavefronts are highlighted in Figure 4. Each EUVI image was processed via a wavelet filter (Stenborg et al. 2008). The images were acquired with a temporal cadence of 2.5 minutes starting from 05:00 UTC to 06:00 UTC. The EUV wave starts (i.e., we see the first signal of a front moving away from the AR) between 05:02:30 and 05:05:00 UTC (Figure 4, frame 1). Within the temporal resolution of the instruments, the EUV wave and the CME result start at the same time (CME starting time as observed by SolO/FSI: 05:00–05:10 UTC; EUV wave starting time as observed by STA/EUVI: 05:02:30–05:05:00 UTC).

Although not as well defined as in STA/EUVI-195, SolO/FSI-174 shows the passage of an EUV wave (Figure 5). The lower definition of these fronts is mainly due to the different wavelength ($\lambda = 174$ Å) used by FSI. Moreover, it is impossible to estimate the starting time of the EUV wave from FSI images because the position of the S/C is

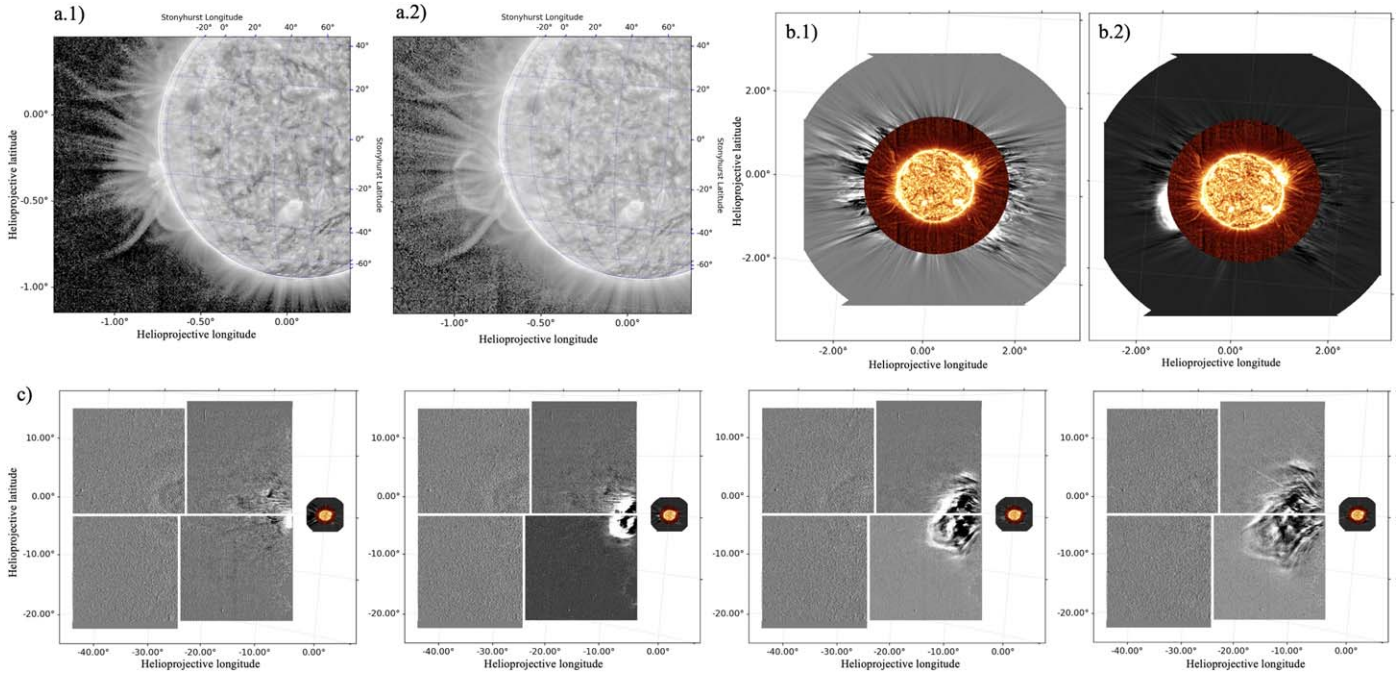

Figure 2. The 2022 March 25 CME as observed by three instruments on SolO during its first close perihelion (≈0.32 au) at ≈05:00 UTC. (a) Images from FSI ($\lambda = 174$ Å) just before the event (a.1, ≈05:00 UTC) and during the first visible CME front (a.2, ≈05:10 UTC). (b) Composite of the FSI-174 image (orange) and the polarized brightness obtained by the Metis coronagraph (gray, $\lambda = 580$–640 nm) showing the corona details just before the event (b.1, ≈05:00 UTC) and when the front reached the Metis internal FOV (b.2, ≈05:30 UTC). (c) Composites of FSI-174, Metis, and SoloHI images at ≈06:20, 07:30, 09:10, and 10:45 UTC. SoloHI follows the evolution of the CME at very large heliocentric distances (>55 $R_\odot$). The CME is clearly visible even after 15:00 UTC. Note: all the Metis and SoloHI images in this figure are a difference of two consecutive images to highlight changes in the complex, evolving CME.

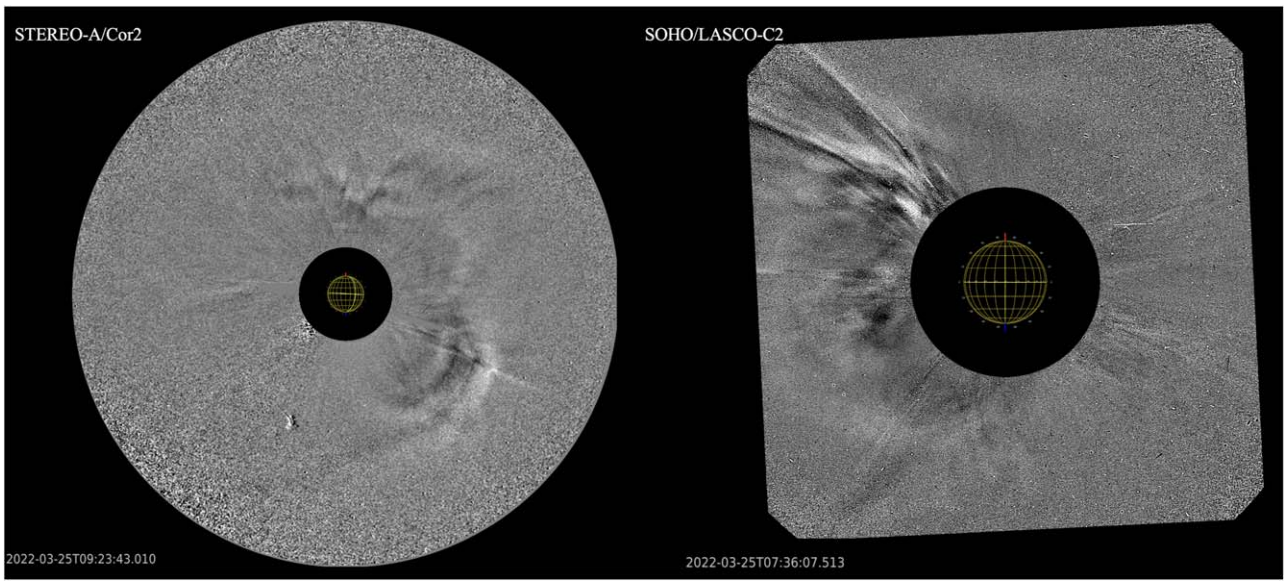

Figure 3. CME as observed by STA/COR2 (left) and SOHO/LASCO-C2 (right). The two S/C were separated by about 33°.

separated in longitude >90° with respect to the origin of the wave. Looking at the STA/EUVI-195 images, we carefully determined the latitude and longitude of the origin of the wave from where the first brightening was observed inside the AR just before the event ($t \approx 04{:}50$ UTC). However, it is possible to clearly observe the front of the CME in its early stage, which is not visible by either STEREO-A or SOHO.

The STA/EUVI position with respect to the AR and its high-cadence observations enables us to perform a kinematics study on the EUV wave propagation (Figure 6). Table 1 summarizes the main characteristics of the observations performed for both the EUV wave and CME by the different considered instruments. In Subsection 3.3, we go into more detail on these aspects and discuss the results.

3.3. CME–Wave Kinematics Analysis

As the first step, we traced the evolution of the EUV wavefront at various position angles (PAs) around its origin through a "point-and-click" method, obtaining the time–distance plot shown in

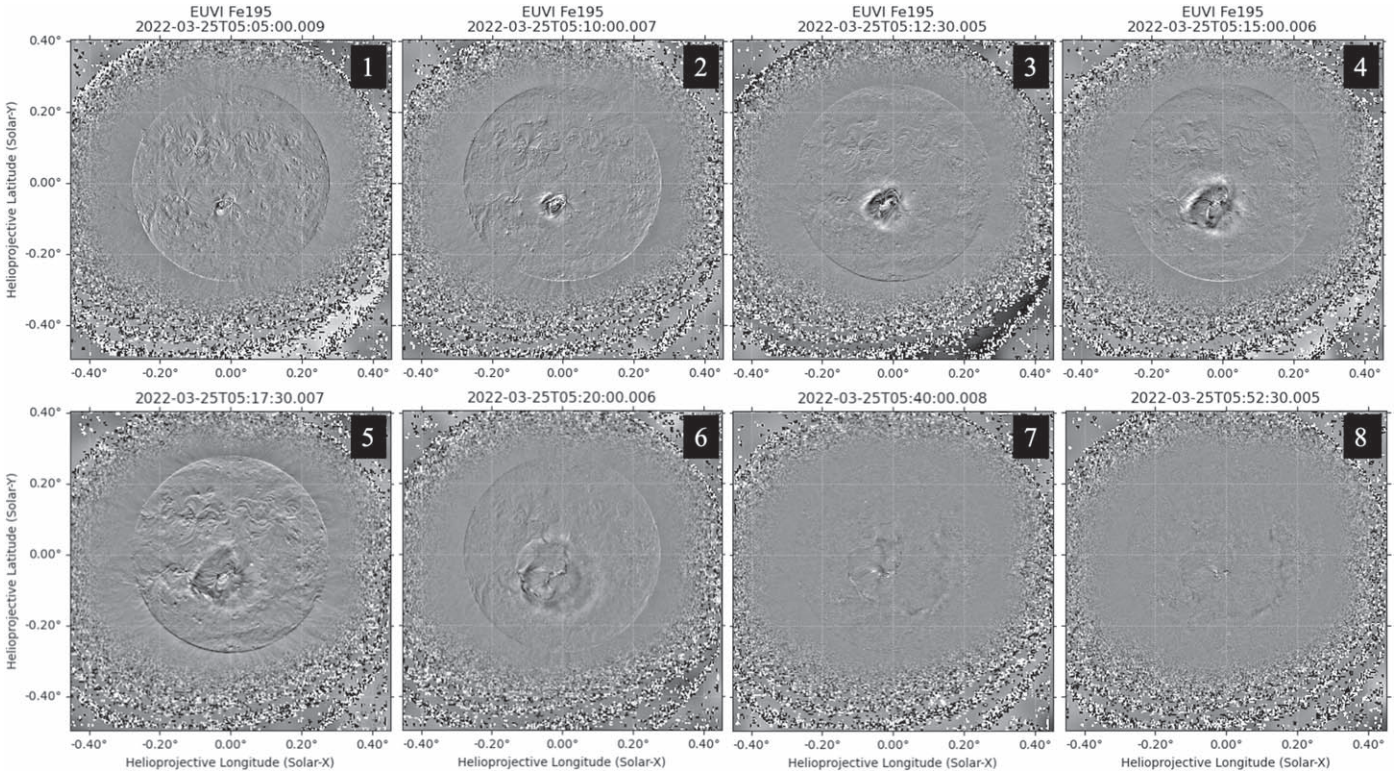

Figure 4. Eight frames from the movie showing the EUV wave evolution as observed by STEREO-A/EUVI-195. Each frame is processed via a wavelet filter (Stenborg et al. 2008; Raouafi & Stenborg 2014) and subtracted by the previous one. The EUV wave starts between 05:02:50 and 05:05:00 UTC and is visible until ≈06:00:00 UTC with a temporal resolution of 2.5 minutes.

(An animation of this figure is available.)

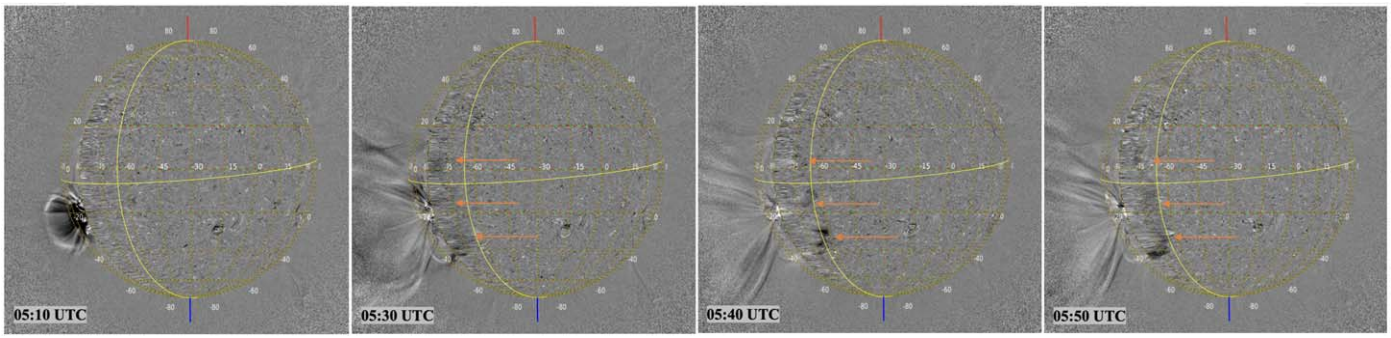

Figure 5. CME and EUV wave (orange arrows) as observed by SolO/FSI-174. Each image is the difference between two consecutive frames. Due to the different wavelength, the EUV wave is not as clearly visible as in STA/EUVI-195. However, it is possible to clearly observe the front of the CME in its early stage (not visible by either STEREO-A or SOHO). The times reported in each frame are in the SolO reference system. To properly compare the wavefront positions observed by SolO with the wavefront positions observed by STEREO-A, we must consider the light travel time between the two S/C. Thus, each SolO frame acquired at a time T must be compared with the STEREO-A frame at $T + 5$ minutes, 20 s.

Figure 6. To evaluate the distances traveled by the front at two instances of time, we applied the haversine formula (Brummelen 2013) to determine the great circle distance between two points (given their longitudes and latitudes) on a sphere of radius $r = R_{\odot}$. From the time–distance plot, it is possible to distinguish three speed regimes: a velocity $v \approx 500\,\mathrm{km\,s^{-1}}$ until 05:20 UTC, $v < 200\,\mathrm{km\,s^{-1}}$ after 05:20 UTC on the west side (i.e., green/yellow/orange lines), and $v < 100\,\mathrm{km\,s^{-1}}$ after 05:20 UTC on the east and north sides (i.e., cyan/blue/dark red lines). These differences originate from the relation of the EUV wave with the CME and the ambient medium. An analogous kinematic study was performed on the wave observed by FSI showing the same behavior of the wave detected by EUVI on the solar west limb (i.e., as expected, the wave observed by FSI is the same one visible by EUVI but from a different point of view).

We also compared, frame by frame, the CME and EUV wave's early phase evolution. Figure 7 shows how the EUV wave on the low corona expands as a wave driven by the lateral expansion of the CME. As suggested by Patsourakos & Vourlidas (2012), the EUV wave behaves as a driven wave as long as the CME expansion speed exceeds the local fast magnetosonic speed. The expansion-driven wave is shown in Figures 7(b.1), (b.2), (c.1), and (c.2). At this time, the CME and EUV wave are still coupled.

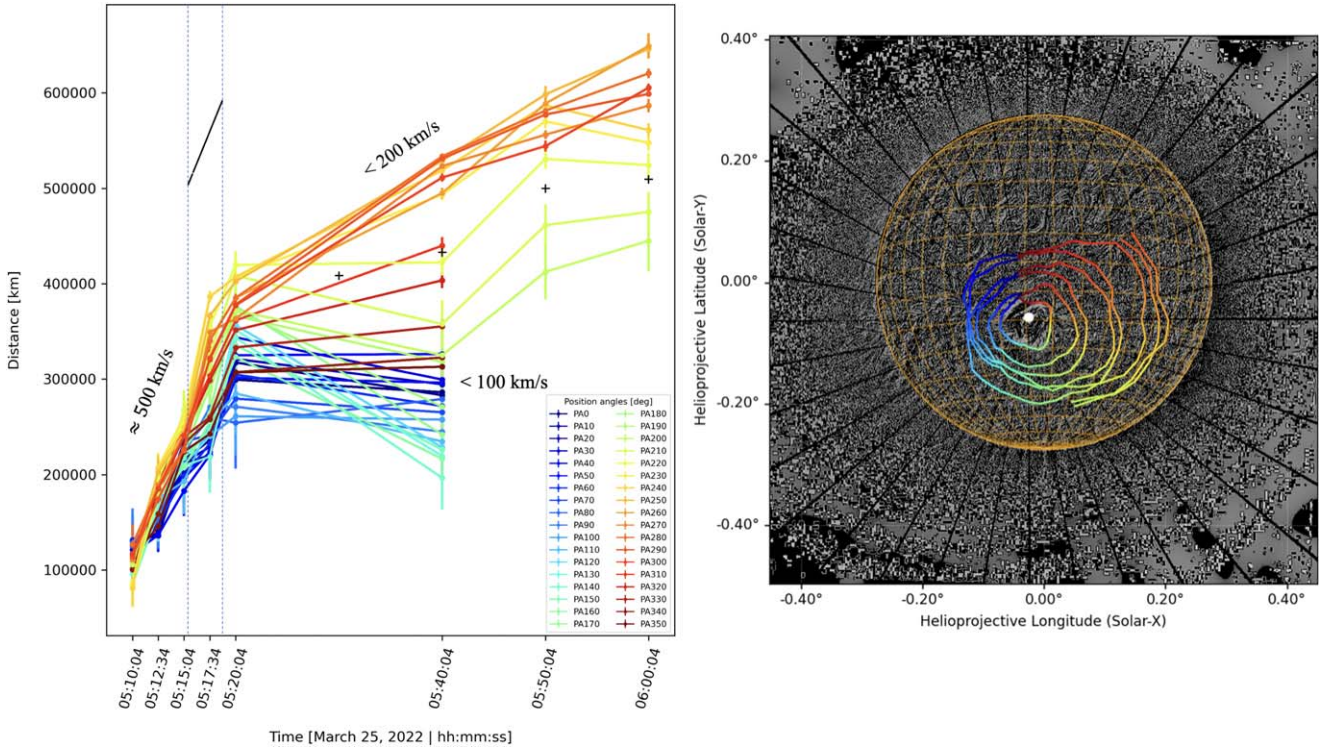

Figure 6. Evolution of the front of the EUV wave in time (left) and space (right). Different colors are different values of position angle (PA): red ≈0°, light blue ≈90°, green ≈180°, and orange ≈270°. The plot on the left shows the distance in time of the EUV front for different PAs. The right image shows the front projected on an EUVI-195 image at a fixed time. The black lines show the considered PAs (36 points separated by 10° each) to outline the front. The error bars are evaluated by performing several times the same process and then evaluating a standard deviation on the measured distances. Negative slopes in the plot indicate a wave reflection. The difficulty in observing the EUV wave at $\lambda = 174$ Å does not allow a similar study with the FSI images. However, the black plus symbols give a qualitative idea of the front position as observed by FSI where the wave is more visible (PA ≈220°). A type II radio burst is observed in the range of time delimited by the two dotted vertical lines. The slope of the black line shows the velocity of the expanding surface (≈450 km s^{-1}) retrieved by from the radio data analysis (subsection 3.4).

Table 1
Cadence and Time Range of the EUV Wave and CME Observation by the Different Instruments

CME	FSI-174	Metis	SoloHI
Cadence obs.	10 minutes	20 minutes	25 minutes
Starting time	05:00/:10 UTC	…	…
End time	…	…	>15:00 UTC
EUV wave	**EUVI-195**		**FSI-174**
Cadence obs.	2.5 minutes		10 minutes
Starting time	05:02:30/:05:00 UTC		…
End time	≈06:00 UTC		≈06:00 UTC

The blue lines in Figures 7(c.1), (c.2) mark the CME front observed by FSI in Figures 7(b.1), (b.2). In particular, the blue lines in Figures 7(c.1), (c.2) are obtained by reprojecting the latitude and longitude of the points along the CME front (Figures 7(b.1), (b.2)) on the EUVI images. Considering the quadrature between SolO and the AR, the longitude of each point of the CME bright front was considered equal to the longitude of the AR. Note that the CME and EUV wave have the same width. Assuming that the CME expands like a sphere in its early phase (i.e., radial expansion = lateral expansion), we find that the driven-EUV wave velocity is consistent with the expansion velocity of the CME in these frames (≈500 km s^{-1}). When the lateral expansion slows, (Figure 7(b.3)), there is a decoupling between the expanding CME and the EUV wave. The EUV wave now propagates freely. Indeed, Figure 7(c.2) shows two fronts: an inner one (the expanding CME) and an outer one (the EUV wave). These two fronts are visible in a base-difference format as well. Because of the combined observations of SolO and STA, we were able to identify the moment when this decoupling happened (between 05:17:30 and 05:20:00 UTC). It is clearly visible also in Figure 6 where, around 05:20 UTC, there is a decrease in velocity due to the fact that the wave is no longer driven by the CME but propagates at its own (lower) speed.

Figure 8 shows the Carrington map with the contour of magnetic field strength calculated from a PFSS model for 2022 March 25 12:04 UTC, 1.2 $R_\odot$; $R_{ss} = 2.5$, where R_{ss} is the source-surface radius. Superimposing the EUV wavefronts (Figure 6), we can see how the wave avoids the strong magnetic field regions or rather, high Alfvén velocity regions (top and top left regions in the figure), while it is free to propagate through the low field regions (right-side regions in the figure). This behavior is consistent with what is expected by the propagation of a fast-mode wave, which refracts away from regions of high propagation speed. The difference in velocity between the east and west sides can be observed in the plot in Figure 6 as well. Indeed the clear division of the velocities in two main blocks after the 05:20 UT is due to this reason; the wave propagating on the east side of the Sun (i.e., cyan/blue/dark red lines, lower velocities) is moving into regions of high propagation speeds and is refracted and potentially reflected away, while the wave propagates without too much distortion on the west side (i.e., green/yellow/orange lines, higher velocities), propagating into regions of lower field/speeds.

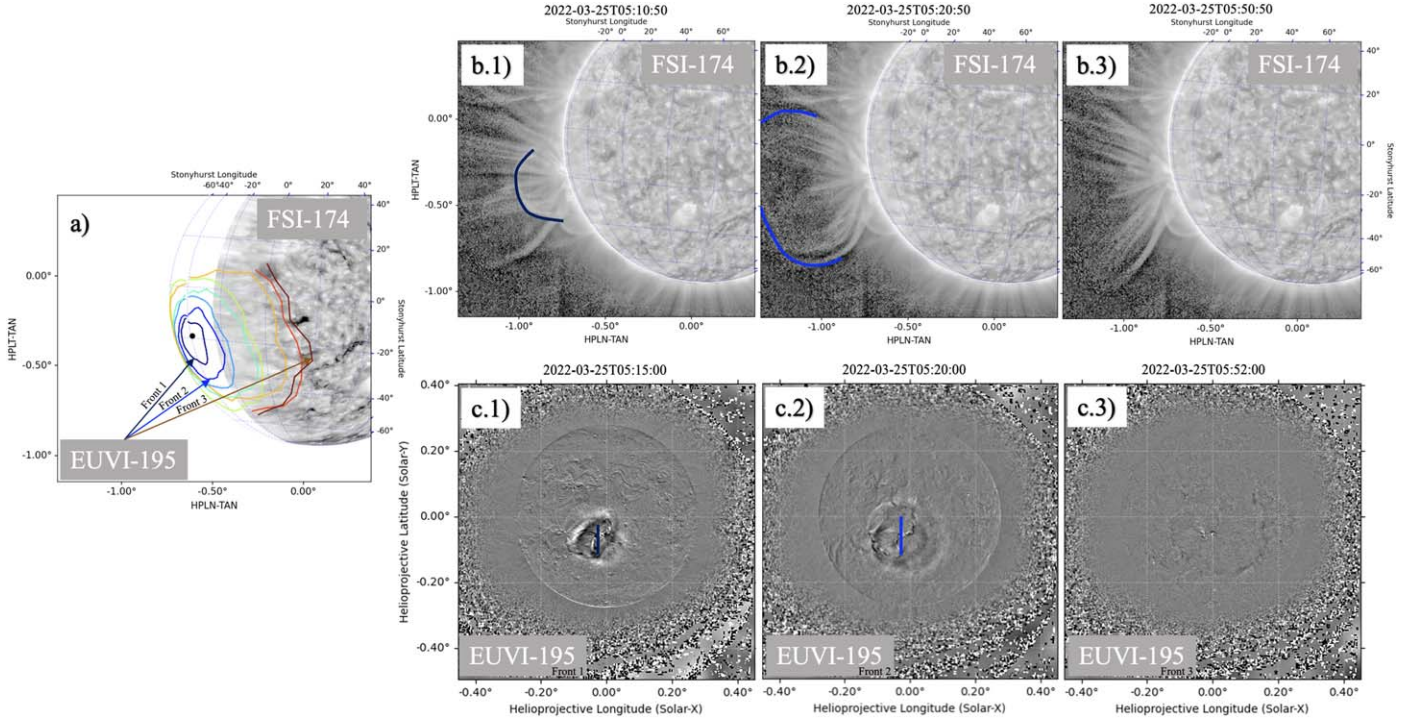

Figure 7. Overview of the EUV wave–CME decoupling. (a) Propagation of the EUV wavefront (as observed by EUVI) in the FSI field of view. (b) Expanding CME as observed by FSI. A huge lateral expansion can be seen by comparing (b.1) and (b.2). The EUV wave is still a driven wave. Moving from (b.2) to (b.3), the CME lateral expansion is almost stopped. We expect to have the decoupling. (c) It is possible to notice the moment of the CME–EUV wave decoupling. Indeed, (c.2) shows two fronts: an inner one (the expanding CME) and an outer one (the EUV wave). (c.2) is the difference between the frames at 05:17:30 and 05:20:00 UTC. The dark blue and blue vertical lines are, respectively, the CME fronts as observed by SolO/FSI in (b.1) and (b.2). Then, from 05:20, the EUV wave is not driven anymore, and we expect to see a decrease in velocity (compare with Figure 6). Finally, (c.3) shows the wave propagating as a fast-mode wave avoiding the high-density regions on the solar east side (Figure 8). Note: the times reported in each frame are in the S/C reference system. To properly compare the wavefront positions observed by STA/EUVI with the CME front positions observed by SolO/FSI, we must consider the light travel time between the two S/C (≈5 minutes, 20 s). For this reason, the closest STA/EUVI frame to the SolO frame at 05:10 is the one at 05:15 UTC.

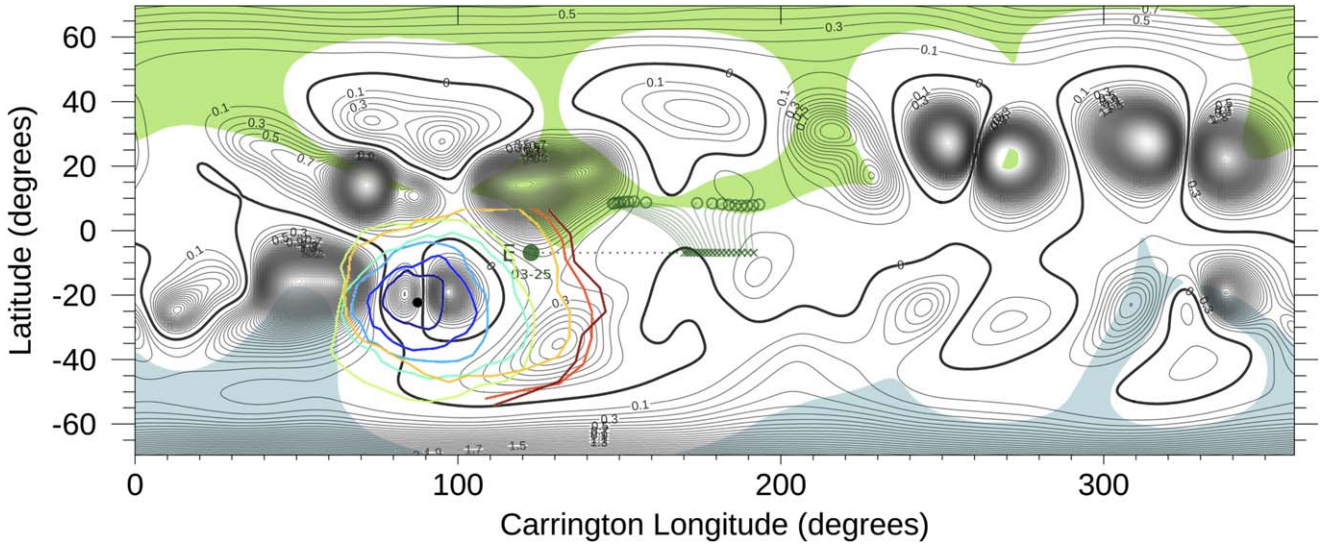

Figure 8. EUV wavefront evolution observed on a Carrington map showing the contour of magnetic field strength calculated from a PFSS model for 2022 March 25 12:04 UTC, 1.2 $R_{\odot}$; $R_{ss} = 2.5$. Notice how the wave seems to avoid strong magnetic field regions (top and top left regions) while being free to propagate through the low field regions (right-side regions). This behavior is consistent with a fast-mode wave. The high-density region close to the ARs does not affect/stop the initial propagation of the wave because, at that time, the wave is a driven wave led by the expansion of the CME. The thick black line on the map shows the predicted heliospheric current sheet, and the blue and green areas are the polar coronal holes with opposite polarity. The dark green dot ("E") shows the position of the Earth (the cross and circle symbols show the regions magnetically connected with the Sun).

These results are consistent with what was obtained by Koukras et al. (2020) and Wang (2000), which show how the fast-mode hypothesis can fit the basic properties of the EUV waves by comparing observations with a ray-path model. In particular, Wang (2000) shows also how the wave is reflected/refracted by strong-field sources.

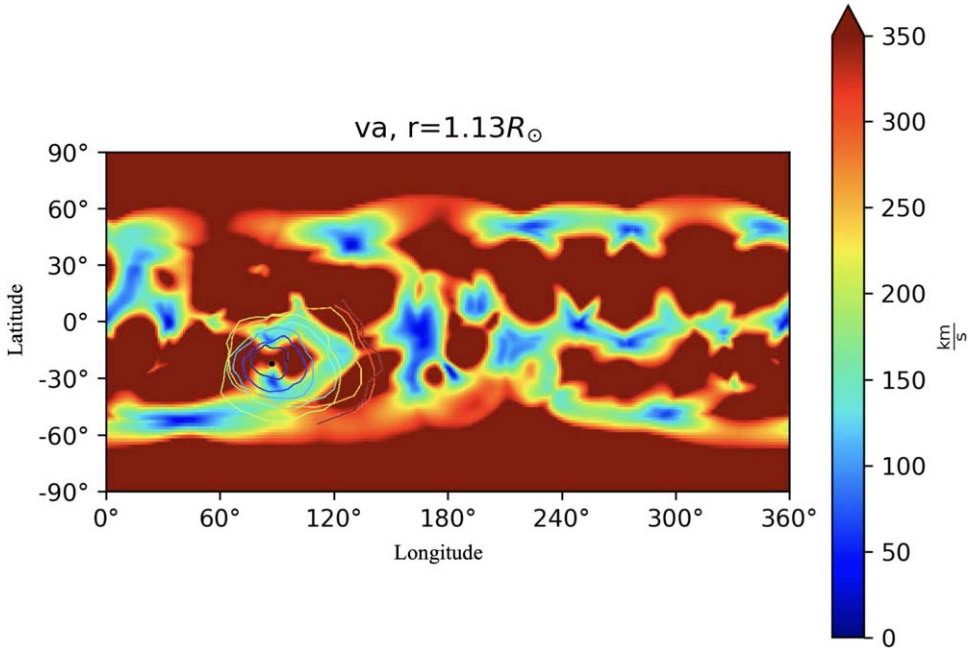

Figure 9. EUV wavefront evolution observed on a map of the Alfvén velocity v_A at different Carrington latitudes and longitudes (from MAS model). The wave propagates with a speed of $v \approx 200\,\mathrm{km\,s^{-1}}$ in regions with Alfvén velocity $v_A < 200\,\mathrm{km\,s^{-1}}$ and stops in regions with much higher v_A (i.e., LN < 60°, LN > 130°–140° and LT < −60°, LT > 0°). This is consistent with the behavior of a fast-mode MHD wave. The initial phases (blue fronts) are associated with the driven phase (see Figure 7).

To be consistent with a fast-mode wave, we expect to have also a local v_A lower than the measured EUV wave velocity (see Subsection 3.1). The EUV wavefronts from Figure 6 are shown in Figure 9 plotted over the v_A contour plot, at a fixed altitude above the solar surface,[8] calculated from the Predictive Science Inc. Magnetohydrodynamic Algorithm outside a Sphere (MAS). The 3D MHD Model[9] is available.[10] The initial phase of the wave propagation (blue/cyan fronts) is still driven by the CME lateral expansion and can propagate independently by the value of v_A. When decoupled from the CME, the wave propagates with a velocity of $\approx 200\,\mathrm{km\,s^{-1}}$ in regions with a local Alfvén velocity $v_A < 200\,\mathrm{km\,s^{-1}}$. Then, when the value of the v_A starts to increase, the wave stops propagating. These results are consistent with the behavior of a fast-mode MHD wave. However, looking at the high Alfvén speed regions at LN ≈ 120°–140° (Figure 9), it is possible to notice that the wave stops just after traveling some distance therein. A fast-mode wave can be refracted and reflected by the high Alfvén velocity regions. The combination of these two factors results in a very short propagation of the wave together with a strong loss in intensity. For this reason, the wave may appear visible but stationary in these regions (last two to three fronts in Figure 9). In any case, we should also consider possible errors in the local density estimation due to the approximations in the model, which can compromise the estimation of the local Alfvén velocities. Indeed, Figure 8, which is based on the magnetic field only, shows a better agreement. Also Wang (2000) highlights how its results critically depend on the 3D distribution of magnetic field and density in the corona.

3.4. Radio Signal Analysis

When the difference between the CME expansion speed and the ambient solar wind in the solar corona is larger than the local fast-mode speed, v_f, solar type II radio bursts may be observed. Type II radio bursts typically appear as bands of enhanced radio emission slowly drifting from high to low frequencies and usually show a fundamental-harmonic structure (i.e., two drifting bands with a frequency ratio of about 2:1).

Radio emissions linked to the present event were detected by both space- and ground-based instruments in different frequency ranges. In this study, we have used ground-based radio spectrograph data obtained with the Compact Astronomical Low-frequency Low-cost Instrument for Spectroscopy in Transportable Observatory (CALLISTO; Benz et al. 2009) ASSA radio spectrometer,[11] located in Australia, with a time resolution of 0.25 s and a frequency range between 15 and 85 MHz. We also used ground-based radio spectrograph data obtained with the USAF Radio Solar Telescope Network[12] spectrometer of the Learmonth Observatory in the 25–180 MHz frequency range. The complete radio dynamic spectrum shown in Figure 10 was integrated with data retrieved at frequencies below 16 MHz by WAVES, the Radio and Plasma Wave Investigation instrument on board the STEREO-A satellite with a temporal resolution of 60 s. In the WAVES dynamic spectrum, the measurements in the 125 kHz–16.025

[8] Since the EUV wave is visible at $\lambda = 195$Å, we expect it is propagating at ≈90 Mm (≈1.1–1.2 $R_\odot$) from the solar surface (Patsourakos & Vourlidas 2012).

[9] More details on the model can be found at the following link: https://www.predsci.com/corona/model_desc.html (accessed 2023 June 26). Coronal model: thermodynamic with heating model 1; universal date and time: 2022 March 25 T05:00 UT; resolution: $nr = 255$, $nt = 143$, $np = 300$; code version: 0.5.7.1acc1.0.

[10] https://www.predsci.com/mhdweb/data_access.php

[11] About CALLISTO ASSA radio spectrometer: http://www.e-callisto.org/ (accessed 2023 June 26).

[12] USAF Radio Solar Telescope Network4 spectrometer data: https://www.ngdc.noaa.gov/stp/space-weather/solar-data/solar-features/solar-radio/ (accessed 2023 June 26).

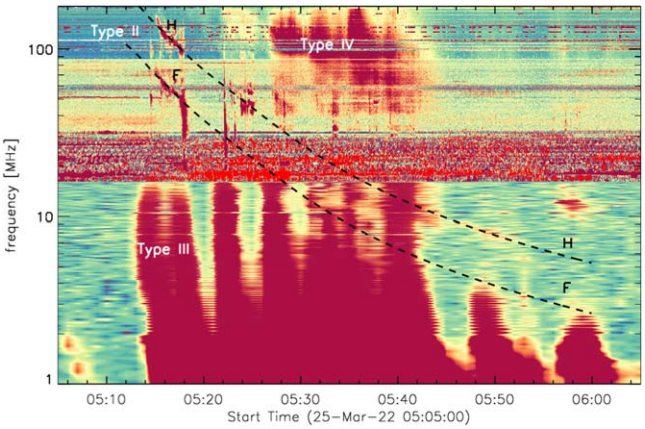

Figure 10. Composite dynamic radio spectrum of the type II radio burst observed on 2022 March 25 obtained by combining ground-based Learmonth e-Callisto ASSA (>16 MHz) and space-based STEREO-A/WAVES (<16 MHz) data. The dashed lines in the figure show the fundamental (F) and harmonic (H) bands as obtained from the density model profiles.

MHz range are from the high-frequency receiver and in the 2.5–160 kHz range from the low-frequency receiver (LFR).

The measured frequency drift rate of the fundamental band at a given time is directly related to the speed v_{sh} of the CME-associated shock and thus provides information on the CME dynamics through the corona, given the electron density radial profile of the background corona in which it propagates. The source cannot be deduced from the radio spectra, however, since the emission can arise from either the shock nose or the flanks so there is always some uncertainty about the derived speeds from radio spectra.

Both type II radio burst fundamental and harmonic emissions were clearly observed in the interval between about 05:15 and 05:18 UTC in the ground-based radio spectrograph.

The MAS model (the same model used to get v_A above) provides also the radial density profile. Assuming radial propagation, we were able to infer (e.g., Mancuso et al. 2019) that the sources of the radio emission of both fundamental and harmonic lanes, observed by the ground-based radio spectrographs in the metric range, outwardly propagated in a coronal region corresponding to a height ranging from $1.25\,R_\odot$ (at 05:15 UTC) to $1.38\,R_\odot$ (at 05:18 UTC), with the shock surface expanding with a speed ranging from about 425 to 470 km s^{-1}. This is consistent with the initial velocity of the expanding CME (Section 2). Thus, looking at these data, we conclude that the expanding CME front caused the type II radio emission (radial expansion; Cairns & Robinson 1987; Bale et al. 1999) and the driven-EUV wave (lateral expansion; Patsourakos & Vourlidas 2012). When the expansion slows (≈05:20 UTC), the radio emission stops, and at the same time, the EUV wave becomes freely propagating.

4. Conclusion and Discussion

On 2022 March 25, several S/C observed a CME propagating away from AR 12974 associated with a global EUV wave. In this paper, we performed a detailed analysis of this event. Making use of the strategic relative position of SolO and STEREO-A (near quadrature), the STEREO-A/EUVI high cadence, and the different remote sensing on board SolO, it was possible to follow the evolution of both the CME and the associated EUV wave to deconstruct their interrelation.

The wave kinematic study clearly shows how the observed EUV wave is best interpreted as a phenomenon that starts as a driven wave on the flanks of the CME (due to a rapid lateral expansion of the associated CME) and then propagates as a fast-mode MHD wave (once the CME lateral expansion ceases) as proposed by Patsourakos & Vourlidas (2009) and Kienreich et al. (2009). The wave propagates away from strong magnetic field/high Alfvén speed regions and propagates preferentially in low Alfvén velocity areas (i.e., $v_f > v_A$) in a quasi-isotropic way, confirming its fast nature. The observation of a double front by STEREO-A, compared with the CME fronts observed by SolO, is also consistent with this interpretation and gives the final remote-sensing proof about the EUV wave/CME relationship. In addition, the analysis of the radio signal adds information on the observed events, showing the presence of a type II radio burst, which is generated by the rapid CME radial expansion (at $\sim 1.25\,R_\odot$). Finally, the radio data give also additional proof of the EUV wave/CME decoupling, showing that the radio signal ceases at the same time that the EUV wave becomes free to propagate.

The large amount of evidence summarized in this study (i.e., imaging, kinematics, radio analysis, and comparison with B and v_A maps) supporting the hybrid interpretation of the EUV wave observed in this event gives further support to the hybrid interpretation of EUV waves proposed by Patsourakos & Vourlidas (2012).

Acknowledgments

The authors want to thank Phil Hess, Guillermo Stenborg, and the entire Solar Orbiter Heliospheric Imager (SoloHI) team for their help and support. We want to thank also Athanasios Kouloumvakos for the helpful discussions and comments on the coronal models. The SoloHI instrument was designed, built, and is now operated by the US Naval Research Laboratory with the support of the NASA Heliophysics Division, Solar Orbiter Collaboration Office under DPR NNG09EK11I. The work of A. L. and P.C.L. was conducted at the Jet Propulsion Laboratory, California Institute of Technology under a contract from NASA (80NM0018D0004). A.V. is supported by NASA grants 80NSSC22K1028 and 80NSSC22K0970. C.R.B. acknowledges the support from the NASA STEREO/SECCHI (NNG17PP27I) program and NASA HGI (80NSSC23K0412) grant. M.V. was supported by ISSI via the J. Geiss fellowship and NASA contracts NNN06AA01C and the NASA Parker Solar Probe Observatory Scientist grant NNX15AF34G.

ORCID iDs

Alessandro Liberatore https://orcid.org/0000-0002-0016-7594
Paulett C. Liewer https://orcid.org/0000-0002-5068-4637
Angelos Vourlidas https://orcid.org/0000-0002-8164-5948
Carlos R. Braga https://orcid.org/0000-0003-1485-9564
Marco Velli https://orcid.org/0000-0002-2381-3106
Olga Panasenco https://orcid.org/0000-0002-4440-7166
Daniele Telloni https://orcid.org/0000-0002-6710-8142
Salvatore Mancuso https://orcid.org/0000-0002-9874-2234

References

Antonucci, E., Romoli, M., Andretta, V., et al. 2020, A&A, 642, A10
Bale, S. D., Reiner, M. J., Bougeret, J.-L., et al. 1999, GeoRL, 26, 1573
Benz, A. O., Monstein, C., Meyer, H., et al. 2009, EM&P, 104, 277
Biesecker, D. A., Myers, D. C., Thompson, B. J., Hammer, D. M., & Vourlidas, A. 2002, ApJ, 569, 1009

Brummelen, G. V. 2013, Heavenly Mathematics: The Forgotten Art of Spherical Trigonometry (Princeton: Princeton Univ. Press)
Cairns, I. H., & Robinson, R. D. 1987, SoPh, 111, 365
Cliver, E. W., Laurenza, M., Storini, M., & Thompson, B. J. 2005, ApJ, 631, 604
Dai, Y., Ding, M. D., Chen, P. F., & Zhang, J. 2012, ApJ, 759, 55
Delaboudinière, J. P., Artzner, G. E., Brunaud, J., et al. 1995, SoPh, 162, 291
Delannée, C., & Aulanier, G. 1999, SoPh, 190, 107
Gieseler, J., Dresing, N., Palmroos, C., et al. 2023, FrASS, 9, 384
Howard, R. A., Vourlidas, A., Colaninno, R. C., et al. 2020, A&A, 642, A13
Kienreich, I. W., Temmer, M., & Veronig, A. M. 2009, ApJL, 703, L118
Koukras, A., Marqué, C., Downs, C., & Dolla, L. 2020, A&A, 644, A90
Long, D. M., Bloomfield, D. S., Chen, P. F., et al. 2017, SoPh, 292, 7
Mancuso, S., Frassati, F., Bemporad, A., & Barghini, D. 2019, A&A, 624, L2
Patsourakos, S., & Vourlidas, A. 2009, ApJL, 700, L182
Patsourakos, S., & Vourlidas, A. 2012, SoPh, 281, 187
Raouafi, N. E., & Stenborg, G. 2014, ApJ, 787, 118
Rochus, P., Auchère, F., Berghmans, D., et al. 2020, A&A, 642, A8
Stenborg, G., Vourlidas, A., & Howard, R. A. 2008, ApJ, 674, 1201
Thompson, B. J., Gurman, J. B., Neupert, W. M., et al. 1999, ApJL, 517, L151
Wang, Y. M. 2000, ApJL, 543, L89